Thermalization in the Quantum Ising Model – Approximations, Limits, and Beyond

Daniel Jaschke,[1] Lincoln D. Carr,[1] and Inés de Vega[2]

[1]*Department of Physics, Colorado School of Mines, Golden, Colorado 80401, USA*
[2]*Department of Physics and Arnold Sommerfeld Center for Theoretical Physics, Ludwig-Maximilians-University Munich, 80333 Munich, Germany*

We present quantitative predictions for quantum simulator experiments on Ising models from trapped ions to Rydberg chains and show how the thermalization, and thus decoherence times, can be controlled by considering common, independent, and end-cap couplings to the bath. We find (i) independent baths enable more rapid thermalization in comparison to a common one; (ii) the thermalization timescale depends strongly on the position in the Ising phase diagram; (iii) for a common bath larger system sizes show a significant slow down in the thermalization process; and (iv) finite-size scaling indicates a subradiance effect slowing thermalization rates toward the infinite spin chain limit. We find it is necessary to treat the full multi-channel Lindblad master equation rather than the commonly used single-channel local Lindblad approximation to make accurate predictions on a classical computer. This method reduces the number of qubits one can practically classical simulate by at least a factor of 4, in turn showing a quantum advantage for such thermalization problems at a factor of 4 smaller qubit number for open quantum systems as opposed to closed ones. Thus, our results encourage open quantum system exploration in noisy intermediate-scale quantum technologies.

I. INTRODUCTION

In statistical mechanics, it is assumed that a many-body quantum system coupled to a thermal bath will thermalize independently of the initial state. Nevertheless, the conditions for thermalization are subtle and need to be questioned for each specific setting [1, 2]. For example, the presence of gaps in the density of states of the bath [3], the existence of symmetries [4], or the emergence of dynamical phase transitions in the thermodynamic limit may affect the thermalization process. Understanding dissipation and thermalization is crucial for quantum technologies, and includes aspects such as the engineering of steady state preparation or the control of quantum decoherence.

The simplest approach to describe the evolution of a quantum system coupled to a thermal bath is the Lindblad master equation [5–9], which preserves mathematical properties of the open system density matrix such as positivity and norm. With this framework, the description of a single-body open system is straightforward, but many-body systems impose challenges that push numerical methods to their performance limit. Indeed, to correctly describe thermalization, the master equation requires an exact diagonalization of the system, such that all transitions between its eigenstates are considered. Hence, the Lindblad equation contains as many terms (or decaying channels) as transitions between the system energy levels. A further simplification is to consider single-channel Lindblad equations, which depend on Lindblad operators that act locally or quasi-locally on each qudit forming the open system. This approach is accurate for situations to describe steady states or when the bath produces a single relevant transition, for instance in weakly interacting qubits. It has been used to analyze transport in spin problems, where a one-dimensional many-body open system couples to baths via both the first and last site [10–13] or to study decoherence in strongly correlated systems [14–17]. However, as shown in [18–21] for single open qubits or qudits, the single-channel approach may not be sufficiently accurate to describe thermalization or even quantum transport [22]. A qualitative reason is that to describe the relaxation of a many-body, or even a multi-level, open system to its thermal state requires the bath redistribute the occupation probabilities of all its energy levels according to a Gibbs distribution. Naturally, this process can only be accounted for correctly when the Lindblad equation produces transitions among all energy levels of the system.

In this work, we consider a harmonic bath weakly coupled to our system. To justify our use of the Lindblad equation, a Born-Markov approximation is considered, in which we take the relaxation timescale of the bath to be very short in comparison to the relaxation timescale of the system. This approximation implies that the bath state only suffers small fluctuations around its

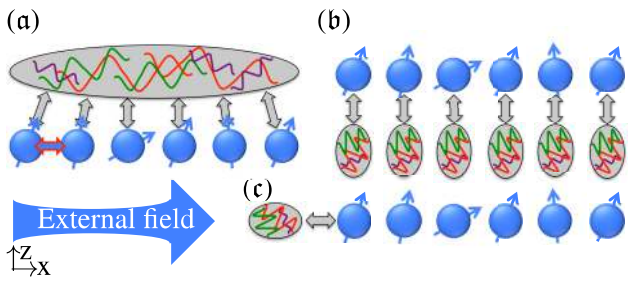

FIG. 1. *Quantum Ising chain coupled to three different baths: common, independent, and end-cap.* The thermalization of the quantum Ising model when coupled to a thermal bath raises many intriguing questions: Will the system thermalize? If so, at what rate? Are there any suitable approximations to model the process in the many-body limit? The system Hamiltonian consists of an external field in the x-direction indicated by the big blue arrow trying to align the spin $1/2$ particles (blue spheres with arrow) in the x-direction to reach the ground state. The nearest-neighbor interaction in the z-direction, highlighted only for the first two sites in (a) competes with the external field in the ground state trying to align neighboring spins. The baths correspond to a three-dimensional electromagnetic field represented by grey ovals with a dense and wide mode spectrum. The grey arrows indicate the interaction with each of the system spins. We consider: (a) a *common* bath coupled to all sites, (b) *independent* baths for each site, and (c) an end-cap scenario in which only the first site is coupled to the bath. Multi-channel Lindblad operators can simulate all three scenarios; neighborhood single-channel Lindblad operators are enabled for scenarios (b) and (c).

thermal initial state, such that only short-time system-bath correlations are considered. A further step to derive the Lindblad equation is to consider the secular approximation, which neglects processes involving large differences between two energy transitions, and which is based on a similar argument as used for the rotating wave approximation.

We further consider that our open system is described by the well-known quantum Ising model [23, 24]. Its equilibrium and dynamical properties have been widely analyzed, including generalizations such as long-range interactions [25–28]. The open quantum system dynamics of 1D spin chains have been studied in an end-cap scenario with the idea of a wire attached to either end, or else a subsystem of a much larger 1D spin chain. This approach amounts to independent baths coupled to both ends of the chain with Lindblad operators constructed in terms of Hermitian Majorana operators [10], or defined in terms of the first two and last two spins as in [11], a proposal recently extended in [13]. The basic aim of these proposals is to drive the system to its thermal state, by imposing a local version of the detailed balance condition. Alternatively, [29] analyzes the same configuration by constructing the Lindblad operators in terms of the system eigenstates, which are computed by assuming periodic boundary conditions. However, a general description of not only the steady state but also the relaxation process of an Ising chain coupled to a thermal bath in different configurations and without periodic conditions has not been done up to now to our knowledge. Such analysis is particularly timely in quantum simulation experiments where, among other spin systems, e.g., the XYZ model [30, 31], as well as Bose- and Fermi-Hubbard models, the Ising model is one of the main models of choice [32]. Trapped ions and Rydberg chains either in optical lattice or optical tweezer arrays can produce Ising chains [33, 34], and generalized Ising models with different couplings such as the chimera map in D-Wave form the basis of practical quantum machines. Thus, understanding the thermalization and decoherence properties of the minimal 1D nearest-neighbor Ising chain is an essential first step. We build this description and extend previous studies in two ways.

First, we analyze three experimentally feasible, distinct scenarios of coupling a bath to an Ising chain as presented in Fig. 1: These are (a) a *common* bath coupled to all sites, thus producing atom-atom interactions, (b) *independent* baths coupled to each site, and (c) a single *end-cap* bath coupled only to the first site in the Ising chain. We determine the resulting timescale for thermalization and discuss how crucial it is to consider the effects of the $\mathbb{Z}_2$ symmetry of the quantum Ising model. For our choice of the interaction Hamiltonian, we find that the Lindblad description preserves the symmetry sectors and, thus, the system thermalizes in each symmetry sector, but not across sectors. This statement excludes results from Secs. IV C 2 and IV E.

Second, we compare a multi-channel Lindblad equation to single-channel Lindblad approaches. The multi-channel case makes no further approximations to the microscopically derived Lindblad equation and, therefore, it correctly describes the system thermalization within such a framework. However, tensor network methods such as matrix product density operators (MPDO) cannot be applied. The multi-channel approach reduces by at least a factor of four the number of qubits that can be treated with respect to the closed quantum system case. Indeed, while exact diagonalization of the Hamiltonian of closed systems is limited to 14 qubits on typical personal computers or laptops, the time evolution of an initial state can be extended to larger systems. Without using parallelization, Krylov and Trotter methods allow for the evolution of at least 24-25 qubits, while parallelization techniques allow one to treat closed systems as quantum circuits of 45 to 64 qubits [35–37]. Hence, the single-channel local approach is commonly used for many-body calculations, since it allows one to employ the same techniques as for the closed system case when evolving a density matrix instead of a pure state. Moreover, MPDO is a highly efficient method to reach much larger systems. To be able to describe thermalization while at the same time keeping the Lindblad equation as local as possible, we propose quasi-local or three-site neighborhood Lindblad operators, where two adjacent spins control the flip of the central one. This operation is known from closed systems as quantum gates, in our case a three qubit extension of the standard CNOT (controlled-not) gate, where an operation on one qubit is based on the state of another qubit. However, we will show that the neighborhood approach only produces accurate results in the extreme paramagnetic or ferromagnetic limits. For the Ising chain anywhere in the proximity of the quantum phase transition, the vital factor of four overhead required for the multi-channel calculation is necessary. In other words, we show that a quantum advantage occurs for at least a factor of four less qubits for open quantum systems as compared to closed ones. For instance, if we supposed quantum advantage for 50 qubits in a closed system, for an open quantum system we only require around 13 qubits. Our results put the emphasis on open quantum system quantum simulators for the nearest term noisy intermediate-scale quantum (NISQ) technology.

The outline of our work is as follows. We introduce the closed and open quantum systems in Sec. II. We continue in Sec. III with a detailed look at our evolution equations. This section includes multi-channel and single-channel Lindblad equations and their properties, such as the eigenvalue decomposition and symmetries. Then, we evaluate the thermalization timescales for different scenarios in Sec. IV. Finally, we discuss possible experimental realizations in Sec. IV F and conclude our results in Sec. V. Some topics we have included as appendices for the interested reader who wishes to consider in detail additional aspects supporting the main study: the odd symmetry sector in App. A; details on the coupling strengths in the multi-channel Lindblad equation as well as in the derivation of the single-channel operators in App. B; and the choice of a different operator in the interaction Hamiltonian in App. D.

II. ISING SPIN CHAINS AND THEIR BATH COUPLINGS

In this section, we remind the reader of the system Hamiltonian, namely the transverse quantum Ising model. We then introduce the different system-bath configurations as well as the models of Lindblad master equation that we will consider. We discuss the common, independent, and end-cap bath scenarios (𝔞), (𝔟), and (𝔠) from Fig. 1.

A. Transverse quantum Ising model

We focus on the transverse quantum Ising model in one dimension with a Hamiltonian given as

$$H_{\mathrm{QI}} = -\sum_{k=1}^{N-1} \cos(\phi)\sigma_k^z\sigma_{k+1}^z - \sum_{k=1}^{N} \sin(\phi)\sigma_k^x\,, \tag{1}$$

where the formulation of the coupling in terms of sine and cosine simplifies addressing the ferromagnetic ($\phi = 0$) and paramagnetic ($\phi = \pi/2$) limit. The system size or the number of qubits in the quantum Ising chain is N. The Pauli spin operators σ_k^x and σ_k^z are acting on site

k, $\cos(\phi) \equiv J/\sqrt{J^2+g^2} > 0$ is the unitless interaction energy, and $\sin(\phi) \equiv g/\sqrt{J^2+g^2}$ is the unitless coupling to the external field. The critical point of the quantum Ising model is at $\phi_c = \pi/4$ for the thermodynamic limit $N \to \infty$, i.e., $\sin(\phi_c) = \cos(\phi_c) = 1/\sqrt{2}$. We treat systems below ten qubits and the position of the minimum of the gap ϕ_c, i.e., an indicator of the quantum critical points, shifts to values $\phi_c < \pi/4$ due to finite-size effects. Note that in this formulation the Hamiltonian $H_{\rm QI}$ is expressed in terms of the $\sqrt{J^2+g^2}$, and all quantities are therefore unitless.

The quantum Ising model has a $\mathbb{Z}_2$ symmetry. This symmetry is very useful when treating the closed quantum system, since it leads to a block-diagonal structure of the Ising Hamiltonian in two blocks representing respectively the even and odd sectors. Furthermore, most of our results are based on choosing an interaction operator $S_k = \sigma_k^x$ that preserves the symmetry, and thus can treat the Lindblad master equation in a particular symmetry sector. In contrast, the choices $S_k = \sigma_k^z + \sigma_k^x$ discussed in Sec. IV E and $S_k = \sigma_k^z$ discussed in App. D do not conserve the symmetry. Reference [38] presents a more detailed discussion of symmetries in the Lindblad master equation.

In the following, we explore the quantum Ising system coupled to a dissipative bath for the common, independent, and end-cap configurations.

B. Coupling to the electromagnetic field in three different configurations

First, we consider the case in which all spins are coupled to a common bath of harmonic oscillators, as described in Fig. 1(a), such that the total Hamiltonian of the system (S) and the bath (R) can be written as

$$H_{\rm S+R}^{(\mathfrak{a})} = H_{\rm QI} + \sum_{k=1}^{N}\sum_{\mathbf{q}} S_k(g_{k\mathbf{q}} b_{\mathbf{q}} + g_{k\mathbf{q}}^* b_{\mathbf{q}}^\dagger) + \sum_{\mathbf{q}} \omega_q n_{\mathbf{q}}\,, \tag{2}$$

where $b_{\mathbf{q}}^\dagger$ ($b_{\mathbf{q}}$) is the creation (annihilation) operator of the bath with a frequency ω_q, and momentum $\mathbf{q}$. Also, $n_{\mathbf{q}} = b_{\mathbf{q}}^\dagger b_{\mathbf{q}}$ is the number operator.

As a second configuration, we consider that each spin is coupled to its independent bath, as described in Fig. 1(b). The total Hamiltonian is

$$H_{\rm S+R}^{(\mathfrak{b})} = H_{\rm QI} + \sum_{k=1}^{N}\sum_{\mathbf{q}} g_{1\mathbf{q}} S_k(b_{kq} + b_{kq}^\dagger) + \sum_{k=1}^{N}\sum_{\mathbf{q}} \omega_q n_{k\mathbf{q}}\,, \tag{3}$$

where now there is a set of harmonic oscillators $b_{kq}^\dagger$ corresponding to the bath attached to each spin k.

Finally, the configuration in Fig. 1(c) corresponds to the case described in Eq. (2) with $g_{k\mathbf{q}} = 0$ for every $k \neq 1$. The interaction Hamiltonian is then reduced to

$$H_{\rm S+R}^{(\mathfrak{c})} = H_{\rm QI} + \sum_{\mathbf{q}} g_{1q} S_1(b_{1\mathbf{q}} + b_{1\mathbf{q}}^\dagger) + \sum_{\mathbf{q}} \omega_q n_{1\mathbf{q}}\,. \tag{4}$$

In all three configurations, the interaction between the system and the bath is modulated by the coupling strength $g_{k\mathbf{q}}$. For the three-dimensional electromagnetic field considered here, such coupling strengths correspond to a dipolar coupling [39],

$$g_{k\mathbf{q}} \sim \sqrt{\hbar\omega_q/(\nu\epsilon_0)}\;(\mathbf{r}_k \cdot \mathbf{d}_{\rm dip})/r_k \exp(-\mathrm{i}\mathbf{r}_k \cdot \mathbf{q}) \tag{5}$$

where ν is the quantization volume. We consider the Planck constant $\hbar$ and the electric permittivity ϵ_0 as unit constants. Furthermore, the coupling $g_{k\mathbf{q}}$ contains the scalar product between the position

of each spin $\mathbf{r}_k$ and the dipole vector $\mathbf{d}_{\rm dip}$, and a different phase factor $\exp(-\mathrm{i}\mathbf{r}_k\mathbf{q})$ for each position and each momentum. Here, we assume that all spins have equal dipole moments and that these are orthogonal to the atomic positions. Atoms are regularly arranged in a chain along the x axis, such that $\mathbf{r}_k = (k-1)a_{\rm lat}\hat{\mathbf{x}}$, with $a_{\rm lat}$ the between adjacent spins in the chain. We note that the same physics described with Eq. (3) can be obtained with the Hamiltonian in Eq. (2), i.e., with a single bath, under particular conditions. This situation is achieved under the condition $q_0^{\rm min} a_{\rm lat} \ll 1$, where $q_0^{\rm min}$ is the resonant wave vector of the field with smallest modulus. Resonant wave vectors correspond to bath modes that interact resonantly with the system frequencies ω, such that $\omega_{q_0} = \omega$. This condition ensures the absence of bath-mediated dipole-dipole interactions between the spins, which therefore evolve as through each of them was coupled to their independent bath.

The interaction Hamiltonian also depends on the system coupling operators S_k, which in most of our examples we choose as $S_k = \sigma_k^x$. We point out that the paramagnetic limit $\phi = \pi/2$ corresponds to a non-interacting model, a case that has been extensibly discussed in [40].

III. DIFFERENT MODELS OF LINDBLAD EQUATIONS

Let us briefly point out in this section the difference between the global multi-channel approach and neighborhood single-channel approach. We use the same Lindblad master equation for both approaches, which we define as

$$\dot{\rho} = -\frac{\mathrm{i}}{\hbar}\left[H,\rho\right] + \sum_{abcd} \mathcal{C}_{abcd}\left(L_{ab}\rho L_{cd}^\dagger - \frac{1}{2}\left\{L_{cd}^\dagger L_{ab},\rho\right\}\right) \qquad \Longleftrightarrow \qquad \frac{\partial}{\partial t}\left|\rho\right\rangle\!\rangle = \mathcal{L}\left|\rho\right\rangle\!\rangle\,, \tag{6}$$

where the formulation with the density matrix ρ (left hand side) or with the super-ket $|\rho\rangle\!\rangle$ in the Liouville space (right hand side) are equivalent. Equation (6) evolves the density matrix ρ of a shape $D \times D$, where D is the dimension of the Hilbert space of the quantum Ising chain. In contrast, the vector representation $|\rho\rangle\!\rangle$ of the density matrix has D^2 entries while the matrix $\mathcal{L}$ acting on $|\rho\rangle\!\rangle$ from the left-hand side is of dimension $D^2 \times D^2$ due to the outer product or Kronecker product, e.g., $H \otimes I$ and I is an identity matrix of size $D \times D$. The Liouville operator is defined as

$$\mathcal{L} = -\frac{\mathrm{i}}{\hbar}\left(H\otimes\mathbb{I} - \mathbb{I}\otimes H^T\right) + \sum_{abcd}\frac{\mathcal{C}_{abcd}}{2}\left(2L_{ab}\otimes L_{cd}^* - L_{cd}^\dagger L_{ab}\otimes\mathbb{I} - \mathbb{I}\otimes L_{ab}^T L_{cd}^*\right)\,, \tag{7}$$

In the Lindblad equation, the Hamiltonian H corresponds to the Hamiltonian of the system and possible corrections from the system-bath interaction. L_{ab} are the Lindblad operators encoding the dissipative part of the dynamics via a transition from state $|b\rangle$ to $|a\rangle$ with a coupling $\mathcal{C}_{abcd}$. Thus, the sum over a, b, c, and d iterates over a set of states. The superscripts T and $*$ are the transpose and complex conjugate of an operator, respectively. Throughout the work, we choose our units such that $d_{\rm dip} = 1$, the lattice spacing $a_{\rm lat} = 1$ between sites, the speed of light $c = 1$, the Boltzmann constant $k_{\rm B} = 1$, and $\hbar = 1$. Thus, the temperature T is implicitly in units of $[J^2+g^2]^{1/2}$ and times are given implicitly in units of $[J^2+g^2]^{-1/2}$. The choice of the Lindblad operators and decay rates depends on the particular case considered. We shall consider two different cases, a multi-channel Lindblad equation as derived from Markov and secular approximations [9], and a single-channel equation with neighborhood single-channel Lindblad operators. These options are detailed in the following.

A. Multi-channel Lindblad equation

In this first approach, we consider the master equation obtained from first principles according to the standard derivation, see [8, 9, 41] for details. This path considers the well-known Born-Markov and secular approximations. A crucial point of this derivation is to diagonalize the system

Hamiltonian, such that

$$H_S = \sum_a E_a \left|a\right\rangle \left\langle a\right| \ . \tag{8}$$

The sum over a contains $d_{\rm loc}^N$ eigenstates without $\mathbb{Z}_2$ symmetry, and $d_{\rm loc}^{N-1}$ eigenstates within a symmetry sector; $d_{\rm loc}$ is the local dimension. This definition allows one to re-express the system coupling operators S_k in terms of such eigenstates,

$$S_k = \sum_{ab} \langle a|S_k|b\rangle L_{ab}. \tag{9}$$

In this representation, the resulting master equation is written in terms of Lindblad operators that represent transitions between different eigenstates, $|b\rangle$ to $|a\rangle$,

$$L_{ab} = \left|a\right\rangle \left\langle b\right| \ , \tag{10}$$

and therefore, the number of Lindblad operators is $d_{\rm loc}^{2N}$ where $d_{\rm loc} = 2$ in our case [1]. Notably, the energy eigenstates can be entangled in the computational basis, i.e., the Fock basis corresponding to the qubits; thus, the state of any spin k' can have different values in the eigenstates $|a\rangle$ and $|b\rangle$ and change during the action of L_{ab}, although the operator in the interaction Hamiltonian acts on site k via $S_k, k \neq k'$. This property contributes to their being named global Lindblad operators.

The decay rates $\mathcal{F}_{abcd}$ in Eq. (6) can be written as

$$\mathcal{C}_{abcd} = \sum_{j=1}^{N}\sum_{k=1}^{N} \mathcal{C}_{abcd}^{[jk]} \ , \qquad \mathcal{C}_{abcd}^{[jk]} = \delta_{E_{ba}-E_{dc}} \gamma^{[jk]}(E_{ba}, E_{dc}). \tag{11}$$

where $E_{ba} = E_b - E_a$ and $E_{dc} = E_d - E_c$ correspond to the two system transitions that are present in each term of the equation. However, the secular approximation considered forces such transitions to correspond to the same frequency, as enforced by the Kronecker delta in Eq. (11). Moreover, the term $\gamma^{[jk]}(E_{ba}, E_{dc})$ depends on the matrix elements of the system coupling operator in the two system transitions,

$$\gamma^{[jk]}(E_{ba}, E_{dc}) = \left\langle a\right| S_j \left|b\right\rangle \left\langle d\right| S_k \left|c\right\rangle \gamma(E_{ba}, \mathbf{r}_{jk}) \, . \tag{12}$$

where $\mathbf{r}_{jk}$ represents the distance between the two spins i and j. This dependency describes the fact that the bath dissipation connects different spins with each others, which gives rise to collective or cooperative effects in the relaxation process. Furthermore, we note that the function $\gamma(E_{ba}, \mathbf{r}_{jk})$ is specific to each type of bath and carries the dependency of the temperature. Here, the bath is a three dimensional electromagnetic field, to which the Ising spins are coupled via the standard dipolar interaction as described by the Hamiltonians (2), (3), and (4) in the three configurations discussed, with the couplings strengths defined in Eq. (5). Because the bath is in the thermal equilibrium, the decay rates fulfill the detailed balance condition, and therefore the steady state of the equation is the thermal state.

Further details of this discussion can be found in App. B.

B. Single-channel Lindblad equation

We propose single-channel Lindblad operators that allow us to express the action of the bath in terms of a number of decaying channels that scales linearly with the number of qubits only. This advantage, together with the fact that they act only either on a qubit or its neighborhood, make

[1] This upper bound could, in theory, be reduced to $d_{\rm loc}^{2N} - 1$, but is not of interest for numerical implementation.

them computationally more feasible. Hence, single-channel Lindblad operators are very useful to describe dissipation in many-body systems without considering the complete energy spectrum, while still transitioning between energy eigenstates in the corresponding limits.

Our design of these operators is inspired by the spectral decomposition described in the previous section. However, the idea is to concentrate on the action of the operator S_k in $|a\rangle\langle a| S_k |b\rangle\langle b|$ on a single site k. To this aim, we use the Schmidt decomposition [42] and rewrite the eigenstates $|a\rangle$ and $|b\rangle$ in terms of a bipartition between the site k and all others sites $\bar{k}$, i.e., all k' with $k' \neq k$,

$$|a\rangle = \sum_i \lambda_{ika} \left|a_k^i\right\rangle \left|a_{\bar{k}}^i\right\rangle , \qquad |b\rangle = \sum_j \lambda'_{jkb} \left|b_k^j\right\rangle \left|b_{\bar{k}}^j\right\rangle . \tag{13}$$

The Schmidt decomposition characterizes the entanglement between two subsystems of a pure quantum state and generates two orthonormal sets of basis states, $\{|a_k^i\rangle\}$ and $\{|a_{\bar{k}}^i\rangle\}$ for each bipartition. The number of components in the Schmidt decomposition depends on the system size and amount of entanglement the state and is therefore not specified. The weight of each basis state within the decomposition is set via the singular values λ_{ika}, which are larger than or equal to zero by definition. With such a decomposition, we can write

$$\begin{aligned} |a\rangle\langle a| S_k |b\rangle\langle b| &= \sum_{ij'} {}^{ij'}\mathcal{F}_{ab}^{[k]} \left|a_k^i\right\rangle \left\langle b_k^{j'}\right| \otimes \left|a_{\bar{k}}^i\right\rangle \left\langle b_{\bar{k}}^{j'}\right| , \\ {}^{ij'}\mathcal{F}_{ab}^{[k]} &= \lambda_{ika}\lambda'_{j'kb} \left(\sum_{i'j} \lambda_{i'ka}\lambda'_{jkb} \left\langle a_k^{i'}\right| S_k \left|b_k^j\right\rangle \cdot \left\langle a_{\bar{k}}^{i'}\middle|b_{\bar{k}}^j\right\rangle \right) . \end{aligned} \tag{14}$$

The coefficient ${}^{ij'}\mathcal{F}_{ab}^{[k]}$ depends on the eigenstates a and b of the system Hamiltonian H_{QI}. Furthermore, the orthonormal basis states of the Schmidt decomposition are denoted by superscripts ij' in front of the symbol.

Building the Lindblad local operators is particularly feasible in the ferromagnetic and paramagnetic limits, since in these limits the eigenstates are not entangled and the Schmidt decomposition contains a single term. In the paramagnetic limit, to observe thermalization we have to choose a coupling operator that is not diagonal to the paramagnetic Hamiltonian, for instance, $S_k = \sigma_k^z$. The corresponding Lindblad operator corresponds to a local spin flip which changes by a quanta the energy of the system. A complete numerical analysis of the dynamics for such a case is presented in App. D. In the ferromagnetic limit, the Lindblad operators have to act on three qubits in order to describe a transition that produces an energy change; we are using the symmetry-broken eigenstates to avoid entanglement in the ferromagnetic limit and, thus, do not use the $\mathbb{Z}_2$ symmetry. More details on the structure and nature of single-channel Lindblad operators is given in App. C.

C. Eigenstate decomposition of the Lindblad equation

It can be analytically shown that a steady state or fixed point of the multi-channel Lindblad equation is the thermal state [9]

$$\rho_{\mathrm{th}} = \frac{\exp\left(-\beta H_S\right)}{Z} , \tag{15}$$

with $\beta = 1/(k_B T)$ and the partition function $Z = \mathrm{Tr}\left[\exp\left(-\beta H_S\right)\right]$, and H_S is the Ising model in our case. However, even with a multi-channel Lindblad equation, the system may not relax to such a thermal state. To analyze this thermalization as well as the decay rates of the system, we take the Lindblad equation in its vector form Eq. (6), and diagonalize the Liouville operator. Since it is not Hermitian, its diagonalization gives rise to left and right eigenvectors. The right eigenvectors, denoted as $|v_j\rangle\rangle$, fulfil the condition $\mathcal{L}|v_j\rangle\rangle = \Lambda_j |v_j\rangle\rangle$, where Λ_j are the corresponding eigenvalues of the Liouville operator $\mathcal{L}$. Thus, the eigenvectors $|v_j\rangle\rangle$ form a complete basis and we can express

any initial density matrix as a linear combination of the basis vectors with some complex weight c_j, i.e., $|\rho(0)\rangle\!\rangle = \sum_j c_j |v_j\rangle\!\rangle$. The time-evolved state can then be written as [43, 44]

$$|\rho(t)\rangle\!\rangle = \sum_j c_j \mathrm{e}^{\Lambda_j t} |v_j\rangle\!\rangle \,, \tag{16}$$

where $c_j = \langle\langle v_j|\rho(0)\rangle\rangle$. On the one hand, the terms corresponding to eigenvalues Λ_j with zero real part do not decay over time and therefore correspond to steady states. Moreover, if there is a single eigenstate with zero real part eigenvalue, this corresponds to the thermal state. On the other hand, the contribution of eigenvectors with a negative real part will vanish within a timescale given by $|\Re(\Lambda_j)|$, where $\Re$ refers to the real part.

If we sort the eigenvalues as $|\Re(\Lambda_j)| \leq |\Re(\Lambda_{j+1})|$, and find only the first one (Λ_0) has a zero real part, the second one $|\Re(\Lambda_1)|$ will define a gap that describes the slowest decay timescale of the system. Further details of the Liouville spectrum have been discussed in literature [38, 43–46].

D. Effects of symmetries

As mentioned before, the Ising model has a $\mathbb{Z}_2$ symmetry that is preserved by the dissipation and divides the Hilbert space into even and odd symmetry sectors. We choose our interaction operator accordingly to ensure the conservation of the symmetry. For simplicity we will perform our analysis within the even sector, which means that instead of analyzing thermalization to a state Eq. (15), we analyze thermalization to

$$\rho_{\mathrm{th}}^{\mathrm{e}} = \frac{\exp\left(-\beta H_S^{\mathrm{e}}\right)}{Z} \,, \tag{17}$$

with H_S^{e} the Ising Hamiltonian in the even sector. We briefly discuss the dynamics within the odd symmetry section in App. D. The use of the symmetry has two advantages.

Firstly, if we do not use the symmetry, we have at minimum two steady states, i.e., one for each symmetry sector. This would give rise to a degeneracy in the steady state eigenstates of the Liouville operator, and therefore to a more complex analysis of the properties of the steady state. Secondly, the symmetry improves the computational scaling. For our spin system, the size of the Liouville operator decreases from $2^{2N} \times 2^{2N}$ to $2^{2(N-1)} \times 2^{2(N-1)}$ which simplifies computational operations such as the eigenvalue decomposition. Therefore, we also have only two sets of $2^{2(N-1)}$ eigenvalues and eigenstates instead of 2^{2N}.

IV. THERMALIZATION TIMESCALES

In the following, we analyze the time evolution of the system and the spectrum of the Liouville operators $\mathcal{L}$. We execute this analysis for the different scenarios of a system-bath coupling sketched in Fig. 1 and represented by the Hamiltonians in Eqs. (2) to (4). We find the timescale for the thermalization of the system for the multi-channel Lindblad operators.

A. Numerical Methods

Our results are based on the exact diagonalization obtained by using the OSMPS package [47, 48]. Without considering symmetries, the number of transitions and decay channels in the Lindblad equation, as well as the dimension of the density matrix, grows in the number of spins as 2^N. Besides considering the time evolution, we analyze the spectrum of the Liouville propagator and study steady states and timescales characterized by the gap in the Liouville propagator. Such an analysis requires diagonalizing a square matrix of dimension 2^{2N}, which is even more limiting. Hence, calculations beyond seven qubits are infeasible without parallelization, and each additional

qubit in the open systems increases the computational resources used by a factor of 64 due to the cubically scaling eigenvalue decomposition. As discussed in the previous section, this scaling is partially improved by the fact that we will be working in the even sector of the $\mathbb{Z}_2$ symmetry.

For a small system of two spins, we analyze the decay by fitting the average of the magnetization, $\bar{\sigma}^x = \frac{1}{N}\sum_{k=1}^{N}\langle\sigma_k^x\rangle$ to a double exponential

$$\bar{\sigma}^x = A_1 \exp(\lambda_1 t) + A_2 \exp(\lambda_2 t) \tag{18}$$

that captures the main decaying timescales. For larger systems the number of timescales involved in the evolution grows exponentially with the number of spins and their contribution will depend on the initial state, which complicates the design of the correct fitting function. Therefore, an alternative is to define the thermalization time as the minimal convergence time to the thermal value of a reference observable,

$$T_{\rm th} = \min_t \left(|\bar{\sigma}^x(t) - \bar{\sigma}^x_{\rm th}| < 10^{-10}\right), \tag{19}$$

or to the thermal state

$$T_{\rm th\mathcal{D}} = \min_t \left(\mathcal{D}(\rho(t), \rho^{\rm e}_{\rm th}) < 10^{-10}\right), \tag{20}$$

where $\mathcal{D}(\rho,\rho') = \frac{1}{2}\|\rho - \rho'\|$ is the trace distance, $\rho^{\rm e}_{\rm th}$ is defined in Eq. (17), and the corresponding expectation value of the average magnetization is $\bar{\sigma}^x_{\rm th}$. We point out that even in the two-qubit case in Fig. 2, the double-exponential fit cannot resolve the two timescales over the full range of ϕ failing for small ϕ. Choosing a relatively tight threshold of 10^{-10} ensures capturing the longest timescales while being definitely above the machine precision of 10^{-14}.

The above thermalization timescales can be related to the real part of the eigenvalues of the Liouville operator. In detail, we can fit the evolution of the trace distance to an exponential

$$\mathcal{D}(\rho(T_{\rm th\mathcal{D}}), \rho^{\rm e}_{\rm th}) = \mathcal{D}((\rho(0), \rho^{\rm e}_{\rm th}) \exp(-\lambda T_{\rm th\mathcal{D}}), \tag{21}$$

which determines the decaying rate as $\lambda \approx |\Re(\Lambda_j)|$. As we will show, the value of j of the eigenvalue will depend on the initial state, which will determine which timescale dominates the decay. In other words, the decay of different initial states will be governed by different eigenstates.

B. Two-site systems

We first consider the case of $N = 2$ and examine the multi-channel Lindblad equation to analyze the common bath (a) with a coupling operator $S_k = \sigma^x$.

Figure 2 shows an analysis of the thermalization time as defined by the convergence of the average mangetization, and starting from a random pure initial state. Figure 2(a) shows that the thermalization time in Eq. (19) increases when approaching to the paramagnetic phase. Since the average magnetization is only evolved up to $\tau = 10$, we find a lack of convergence for $\phi \gtrsim 0.9 \times \pi/2$ as shown by the region in white color. The thermalization time $T_{\rm th\mathcal{D}}$ defined in Eq. (20) yields a different result, as it corresponds to a stricter criterion for thermalization. The maximal difference between the two definitions for all data points with a thermalization time smaller than τ is 3.75. While the magnetization, e.g., $\bar{\sigma}^x$ in the x-direction from Eq. (19), is more useful with regards to experiments, we will use the trace distance $\mathcal{D}$ for further calculations. Figure 2(b) displays the evolution of the x-magnetization at a temperature $T = 0.11$ over time, showing how the relaxation slows down when approaching the paramagnetic limit.

Figure 3 displays the analysis of the eigenstates of the Liouville operator for the same case. Indeed, all decay rates consistently vanish toward the paramagnetic limit. For our coupling operator σ^x, this behavior corresponds to a pure dephasing case where the system does not thermalize. As a consequence, the gaps between all eigenstates in the Liouville operator close toward such a limit and the eigenstates reach full degeneracy.

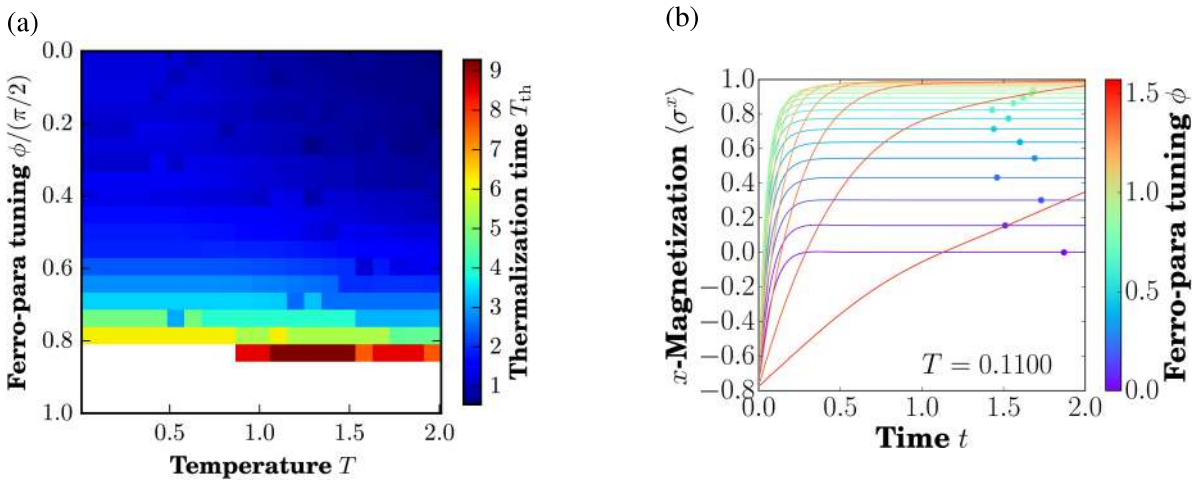

FIG. 2. *Thermalization timescales for the multi-channel Lindblad operators with a common bath.* We consider $N = 2$ qubits and start from an initial random pure state. (a) The thermalization time necessary to approach the steady state value of the magnetization according to Eq. (19). (b) The local magnetization plotted over time for $T = 0.11$ describes the transient behavior to the steady state value. Circles indicate the time where the magnetization is first within our tolerance to the steady state value.

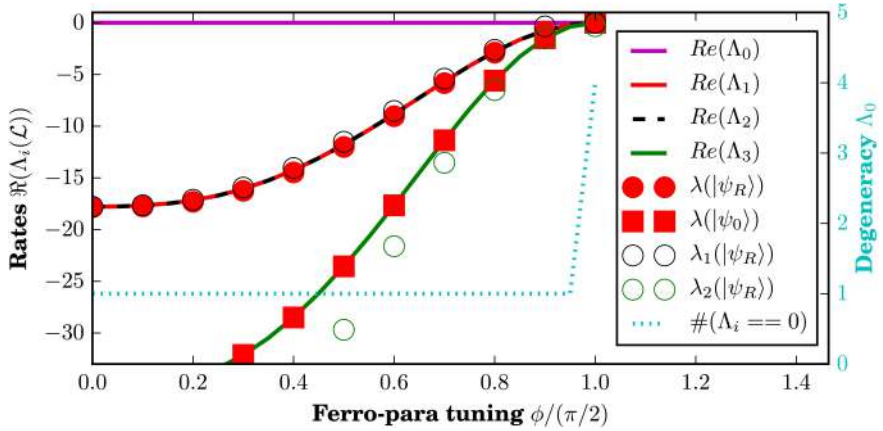

FIG. 3. *Spectrum of the Liouville operator for the global multi-channel Lindblad operators with a common bath.* The spectrum of the Liouville operator for $N = 2$, which defines the thermalization timescale.

We now analyze the Liouville spectrum corresponding to the multi-channel Lindblad equation. The curves in Fig. 3 show that there is a single eigenvalue Λ_0 with a real part that vanishes across the whole parameter space. This property means that within our symmetry sector there is a single steady state for the evolution. Furthermore, the figure displays all other decay rates, which correspond to the eigenvalues $\Lambda_j, j > 0$. We observe that the rates all decay toward the paramagnetic limit, where a full degeneracy is obtained. Indeed, this limit corresponds to pure dephasing where the system does not thermalize. To analyze the dependency of the decay with the initial states, we first consider a random initial state $|\psi_R\rangle$. The empty circles show the rates $\lambda_{1,2}$ that result from the fitting Eq. (18) to the evolution of the average magnetization. The filled circles show the timescale extracted from the trace distance according to Eq. (21) and considering the same random initial state $|\psi_R\rangle$, while the filled squares shows the same for an initial ground state $|\psi_0\rangle$. Notably, the decay of the random initial state is governed by Λ_1, while the decay of the ground state does not depend on the slower timescale and is governed by Λ_2.

C. Beyond two-site systems

We now turn to a more complete analysis that goes beyond the two-site system and consider system sizes up to seven sites in the even symmetry sector. While still considering a coupling operator σ^x, we investigate how the system size affects the thermalization timescale. We investigate how the coupling scheme affects the thermalization. We question the accuracy of considering neighborhood single-channels Lindblad operators. In this analysis, we first consider the multi-channel approach, and then the single-channel approach.

1. *Thermalization for multi-channel Lindblad operators*

Figure 4(a) shows the smallest values $|\Re(\Lambda_i)|$, excluding the steady state, in the spectrum of the Liouville operator $\mathcal{L}$ of the common bath for $N \in \{2, 3, 4, 5, 6, 7\}$. We observe that the gap of the Liouville operator decreases for increasing system size, leading to slower thermalization timescales for larger system sizes. Interestingly, we have observed that this trend also occurs when considering other decay rates different than the ones given later in the appendix by Eq. (B2), although we do not present these details here for brevity. As will be further discussed in Sec. IV D, this observation suggests the presence of subradiance in the emission.

Figure 4(b) shows the thermalization times for different system-bath coupling schemes with $N = 4$ and $T = 0.51$. The thermalization timescales grow for common, independent, and end-cap scenarios as one gets closer to the paramagnetic limit, where the thermalization time approaches infinity. Toward the ferromagnetic limit the thermalization grows more rapid. Moreover, the independent and end-cap scenarios (𝔟) and (𝔠) thermalize faster than with a single common bath (𝔞). Such a common bath introduces spin-spin interactions mediated by the field which in our case slows down the thermalization process, and as we will see, even more as the number of spins in the spin chain grows. Also, we find that the decay of spins initially in the ground state is faster than for an initial random state. However, these differences are more relevant for spins coupled to independent baths than coupled to a common bath. In addition, when the end-cap configuration (𝔠) is initially in the ground state its decay time is exactly the same as the slowest decay of (𝔟).

Figures 4(c) and (d), corresponding to the common and the independent baths, respectively, show that the qualitative behavior of the slowest thermalization rate $\Re\{\Lambda_1\}$ with ϕ is the same for all temperatures T. In both cases, we observe a faster thermalization toward the ferromagnetic limit, but the common bath case shows additionally the presence of a second gap minimum around $\phi = 0.3 \times \pi/2$ for high temperatures starting around $T \geq 0.51$.

The observed features can be experimentally exploited in two possible directions. On the one hand, a common bath and an initial random state will slow down dissipation and decoherence processes when they are not desired, like in certain quantum information schemes. On the other hand, independent baths and initial ground states can be used in situations where a thermal state should be reached as fast as possible. However, we note that the dependence of the thermalization time on the initial state could be different for low temperatures, since the ground state is much closer to the thermal state than an excited one. We dedicate Sec. IV D to a finite-size scaling where we estimate the timescale beyond seven qubits.

2. *Thermalization for single-channel Lindblad operators*

To analyze the feasibility of using neighborhood single-channels to simulate thermalization, we focus on the independent bath configuration (𝔟) and $N = 4$. We do not use the $\mathbb{Z}_2$ symmetry for these calculations.

In Fig. 5(a), we consider the ferromagnetic single-channel Lindblad operators derived in App. C 2 to evolve a random initial state until a time $\tau = 10$ and plot its trace distance to the thermal state. We set the minimal trace distance to 10^{-3} for a meaningful coloring away from the ferromagnetic limit $\phi = 0$. As expected, the simple single-channel approach makes the system converge to the thermal state in the ferromagnetic limit, and it does so down to a trace distance of 10^{-14}. We observe that we reach relatively small trace distances to the thermal state of 10^{-2} for

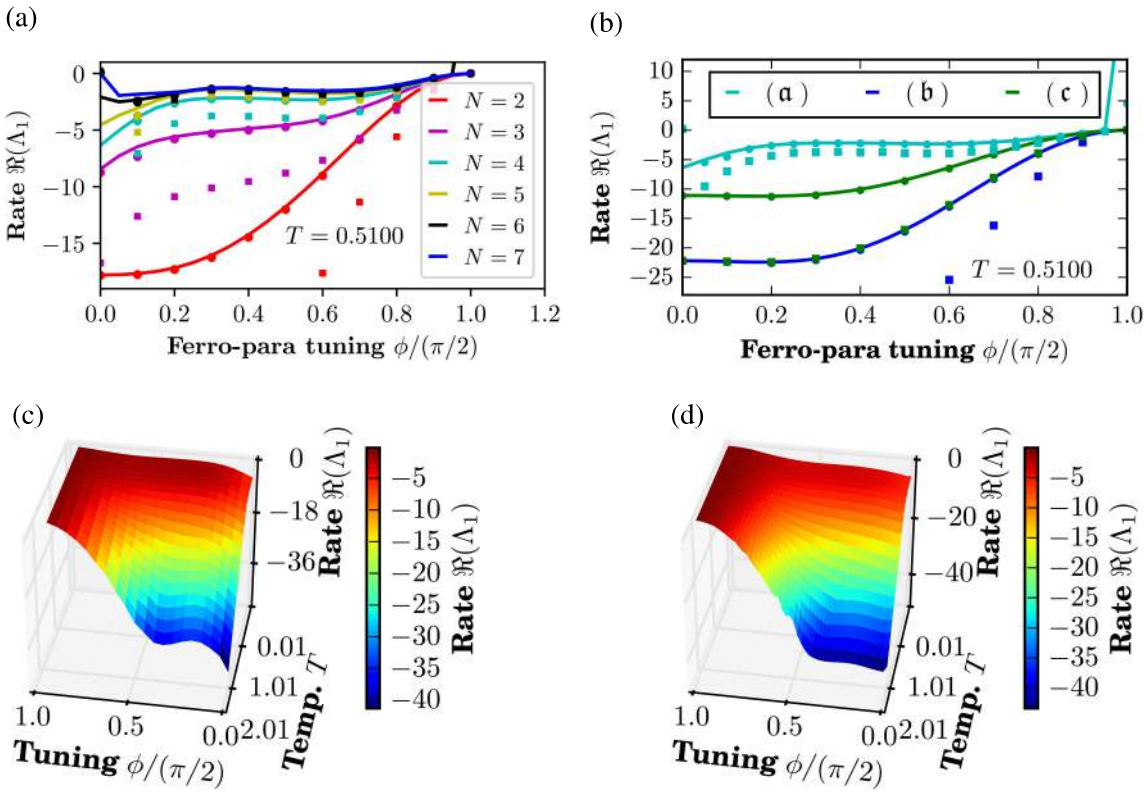

FIG. 4. *Thermalization rates for different systems with multi-channel Lindblad operators.* (a) Decay rates for (𝔞) for $N = 2$ to $N = 7$ spins. Solid curves represent the smaller rate $\Re\{\Lambda_1\}$ obtained from the Liouville spectrum. Circles (squares) represent the decay rate extracted from the trace distance to the thermal state starting from a random state (the ground state) in a time evolution. For numerical constraints, data for $N = 7$ does not include time evolutions. (b) The rates for different system-bath coupling schemes (𝔞), (𝔟), and (𝔠) for $N = 4$ spins. Solid curves, circles, and squares as in (a). (c) Smaller rate $\Re\{\Delta_1\}$ for $N = 4$ across different temperatures T and values for ϕ for the common bath (𝔞). (d) Smaller rate $\Re\{\Delta_1\}$ for $N = 4$ across different temperatures T and values for ϕ for independent baths (𝔟).

small perturbations of $\phi \lesssim 0.032 \times \pi/2$ around the ferromagnetic limit. However, the neighborhood single-channel approach is not valid away from the limiting case. Moreover, we observe that for temperatures $T \leq 0.8$, the system does not thermalize even in the ferromagnetic limit. The reason for this observation is the trace distance has been calculated at a time $\tau = 10$ in which the system might not have thermalized yet, predicting very long thermalization times indeed.

Figure 5(b) shows that the gap of the single-channel Liouville operator $\Re(\Lambda_1)$ decreases for smaller temperatures, which confirms that a time $\tau = 10$ is not sufficent to reach the thermal state in (a) for low temperatures. However, we should stress that the same argument does imply that, away from the small region around $\phi = 0$, the system would thermalize when considering longer times. Indeed, the rate $\Re(\Lambda_1)$ indicates a fast convergence to a steady state, but nevertheless this state does not correspond to the thermal one, which marks the failure of the neighborhood single-channel Lindblad operators beyond the extreme ferromagnetic limit.

Appendix D shows numerical results for neighborhood single-channel Lindblad operators in the paramagnetic limit and we obtain similar results. In conclusion, the approximation is not very useful for solving thermalization problems.

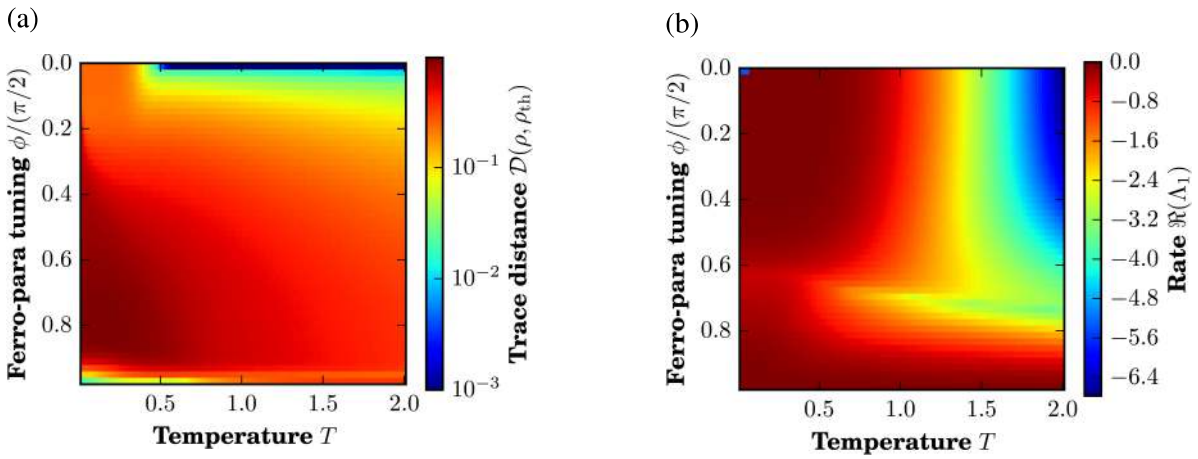

FIG. 5. *Neighborhood single-channel Lindblad operators.* Three-site Lindblad operators designed for the ferromagnetic limit thermalize in scenario (b) only in a very small region around the ferromagnetic limit, and the multi-channel Lindblad operators are the only way to thermalize the system in the complete range of the phase diagram. (a) The trace distance between the time-evolved quantum state and the thermal state at the end of the time evolution with $\tau = 10$ shows thermalization around the limit $\phi = 0$. (b) The rate given by the eigenvalues of the Liouville operator answers the question as to whether the time-evolved state in (a) approaches the thermal state at $\tau = 10$ due to long timescales or due to the failure of the neighborhood single-channel approach.

D. The thermodyanmic limit via finite-size scaling and subradiance

Finally, we approach larger systems with $N > 7$ via finite size-scaling for the data points shown in the previous analysis. We observe that the results for the timescale extracted from the Liouville operator $\mathcal{L}$ converge for the system sizes of five to seven qubits, i.e., the difference is hardly visible in the plots. We use a power-law fitting function of form

$$\Re(\Lambda_{1,N}) = \Re(\Lambda_{1,N=\infty}) - \frac{c'}{N^{c''}}\,, \tag{22}$$

where c' and c'' are positive parameters in the fit that depend on the parameter ϕ within the phase diagram. This approach is established for the analysis of quantum critical phenomena in finite-size systems [24, 49]; the standard deviation obtained from the fit is a good indicator of whether the procedure works for the problem given here. The extrapolation for the thermodynamic limit in Fig. 6(a) suggests a non-zero value for the rate for $N \to \infty$. In addition, it can be seen that within the standard deviation, the features present in the rate for seven qubits are also present in our finite-size scaling result. Thus, our method is promising to analyze the system dynamics for large open systems beyond the limit of exact diagonalization.

We have previously seen in Fig. 4(b) that the decay rate for $N = 4$ is smaller for a system coupled to a common bath than for a system coupled to independent baths. Now, we observe in Fig. 6(a) that for a common bath the decay rate decreases with N. Both features suggest the presence of subradiance, a cooperative phenomenon that leads N spins or atoms to decay much slower than a single atom [50]. Classically the subradiance is described as a result of radiation trapping, i.e., continuous emission and reabsorption by the atomic sample that leads to a slowing down of the irreversible energy loss. In the quantum picture, it is furthermore explained by destructive interference [51].

The phenomenon of subradiance was originally described in quantum optics for independent, i.e., non-correlated atoms; the decay rate of N atoms coupled to independent baths is the same one as for a single atom, $\Gamma_N = \Gamma_1$, while for atoms coupled to a common bath it can either be enhanced (superradiance) or diminished (subradiance) by a factor dependent on N. In the case of

subradiance, the decay time of N atoms τ_N has been related to the single atom decay rate τ_{at} by the relation $\tau_N/\tau_1 = 1 + ab_0$, where a is a constant and b_0 is the atomic optical depth [51].

In our case, the presence of correlations in the system presents two differences with respect to the standard picture. First, even for independent baths the decay rate may depend on N, which we do not investigate here. Second, the dependency of the rate on N may be related to the point of the phase diagram of the open system. Indeed, we can rewrite Eq. (22) as

$$\frac{\Gamma_N}{\Gamma_1} = 1 + \frac{c'}{\Gamma_1}\left(\frac{1}{N^{c''}} - 1\right), \tag{23}$$

where $\Gamma_1 = \Gamma_\infty + c'$. This equation yields a relationship between decay times, τ_1/τ_N since $\tau_N = 1/\Gamma_N$. Through the dependency with c' and c'', we find the equation that relates the decay time for N spins to that of a single one depends on the value of ϕ, and therefore the amount of correlations within the spins. While few works describe collective effects for atoms that are coupled through a hopping term [52–54], even fewer studies describe the effect of atom correlations, like for instance in the context of one-dimensional waveguides [55] or considering just two atoms [56]. Therefore, the interplay between strong correlations and collective effects in the dynamics of many body systems is still a largely unexplored domain.

E. Two coupling operators in the interaction Hamiltonian

We have seen in the previous sections that the relaxation dynamics is highly sensitive to the parameters and structure of both system and interaction Hamiltonians. To illustrate this observation further, we end our analysis by extending beyond our previous common bath scenario. We take the interaction Hamiltonian to include not just one but two coupling operators, namely σ_k^x and σ_k^z, such that we have a final scenario referred as $(\mathfrak{d})$,

$$H_{\mathrm{S+R}}^{(\mathfrak{d})} = H_{\mathrm{z,S+R}} + H_{\mathrm{x,S+R}} = \sum_{k=1}^{N}\sum_{\mathbf{q}}\sum_{\alpha\in\{x,z\}} \sigma_k^\alpha (g_{k\mathbf{q}} b_{\mathbf{q}} + g_{k\mathbf{q}}^* b_{\mathbf{q}}^\dagger)\,. \tag{24}$$

Figure 6(b) contains the first two eigenvalues of the Liouvillian for two to five qubits. Since the $\mathbb{Z}_2$ symmetry is broken by the operator σ_k^z in the interaction Hamiltonian, thermalization occurs in the whole Hilbert space for every parameter regime. An exception is the ferromagnetic limit ($\phi = 0$), where the gap for the first eigenvalue closes. In the ferromagnetic limit, the σ_k^z part in the interaction Hamiltonian is responsible for breaking the symmetry; this part commutes with the system Hamiltonian. It follows that the terms does not produce any transition between eigenstates with different energies, using moreover the properties of the Pauli matrices. It contributes in the Lindblad equation with a term proportional to $\gamma(E_{ba} = 0, \mathbf{r}_{jk})$. However, as discussed in App. B, $\gamma(0, \mathbf{r}_{jk}) = 0$ in our case. Thus in this limit, the term $H_{\mathrm{z,S+R}}$ does not contribute at all to the dynamics. In other words, the system evolution is determined only by $H_{\mathrm{x,S+R}}$, which preserves the symmetry. This reasoning explains the double degeneracy of the ground states of the Liouville operator (with two eigenvalues $\Re\{\Lambda_0\} = \Re\{\Lambda_1\} = 0$), while the finite non-zero value of $\Re\{\Lambda_2\}$ leads to the conclusion that each symmetry sector thermalizes.

F. Experimental realizations

Quantum simulator platforms realizing the quantum Ising model include ultracold atoms and molecules [30, 57], trapped ions [33], and Rydberg systems [34]. Modelling the bath coupled to these architectures or even understanding the accuracy of the Lindblad description are difficult problems on their own. Here we have considered for simplicity a bath consisting of a three-dimensional electromagnetic field present in AMO-based (atomic, molecular, and optical) quantum simulator platforms, which couples to the spins of our system via dipole interactions. The

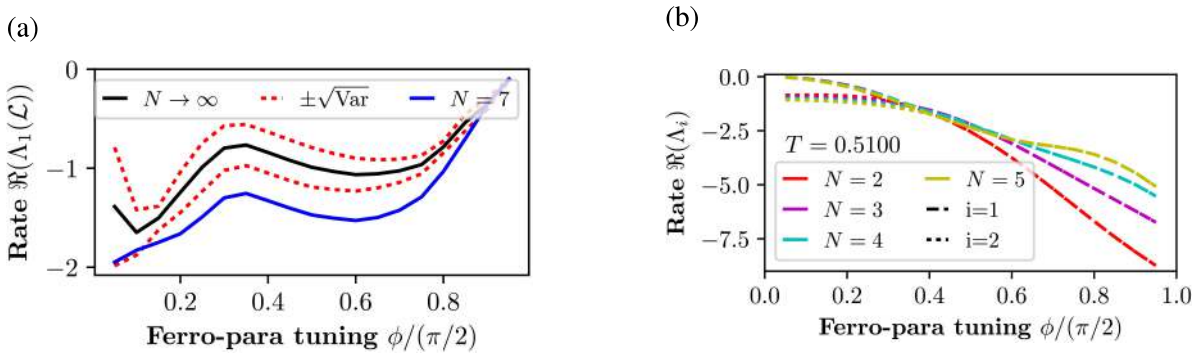

FIG. 6. *Subradiance and generalized coupling.* (a) Finite-size scaling extrapolates the gap of the Liouville operator for system sizes $N \to \infty$. This approach predicts an open gap of the Liouville operator $\mathcal{L}$ toward the thermodynamic limit (including taking the variance of the fit into consideration). For comparison, we show the result for $N = 7$. We hypothesize a subradiance effect. (b) Treating a final bath case ($\mathfrak{d}$), we find for multiple system-bath coupling operators $\sigma^x + \sigma^z$ in the interaction Hamiltonian the system thermalizes across the complete phase diagram except in the limit $\phi = 0$. Thermalization times are deduced from the eigenvalues $\Re(\Lambda_1)$ and $\Re(\Lambda_2)$ of $\mathcal{L}$. System sizes are color coded. First ($i = 1$, dot-dashed) and second ($i = 2$, dotted) non-zero eigenvalues are indicated by line style. Curves may overlap.

black-body radiation of the surrounding experiment can serve as motivation to choose such a field. In addition, trapped ions [58], Rydberg atoms [59] and ultracold atoms [60] can be confined in an optical cavity considered in the bad cavity limit, where the electromagnetic field has a broad-band density of states and therefore produces the desired Markovian interaction [61].

Although we use the electromagnetic field as a basis throughout the paper, a set of interacting spins coupled to a continuous bosonic bath can be implemented with other models. One possibility is to consider ultracold atoms coupled to the bosonic field formed by the excitations of a Bose-Einstein condensate (BEC) as proposed in [62] and extended in [63] for the Ising model. A close alternative is to consider atoms with two internal levels. The first level is trapped by an optical lattice and implements the open system dynamics. The second level is untrapped and plays the role of a bath [64, 65]. Similarly, recent progress has enabled the coupling of qubits to acoustic phonons in superconducting qubits [66], although the long coherence times between qubit and phonon modes cannot be accurately described with our approach based on the Born-Markov approximations. However, both BEC excitations at low momenta [67] and acoustic phonons have a linear dispersion, analogous to photons in the electromagnetic field. This analogy draws the similarity to the model here studied and further emphasizes the experimental applicability of our work.

V. CONCLUSIONS

We have analyzed the dynamics of a quantum Ising model coupled to a thermal field in the Markov limit by considering a multi-channel Lindblad equation, in particular thermalization and decoherence times. Correct calculation of decoherence times is vital to accuracy and verifiability of any quantum simulator, including the many experimental examples treating the quantum Ising model. Such a multi-channel Lindblad equation satisfies the Born-Markov and secular approximations well known to Lindblad approaches and makes no further approximation. In contrast, we have found that the commonly used single-channel or local approximation produces no thermalization in the simulations for the quantum Ising model; thermalization timescales cannot be predicted with this approach.

We explored coupling with the bath in three different experimental scenarios, i.e., common, independent, and end-cap baths. We also explored how thermalization times depend on both the phase diagram and the number of spins in our system. We showed how the bath, system size, and region in the phase diagram can work together to speed up or slow down thermalization, which can be used to protect many-body states from decoherence. For instance, one could quench the system

into a system-bath-phase region protected from decoherence and reverse the quench to regain the state when needed. The errors introduced due to non-adiabatic quenches might be less critical than the errors from decoherence while storing the state for a long time. We emphasize that very little is known about control of many-body decoherence, with most decoherence times given in terms of one or a few qubits subject to gate operations in a "digital" quantum computer, and scaling to larger systems assumed, a well-known problem in trapped ions, for example. In contrast, our study applies directly to calculations on "analog" quantum computers, i.e., quantum simulators, as well as to adiabatic quantum machines like D-Wave. Our study can also shed light on the coherence times of large many-body states in digital quantum computers between gate operations.

In detail, we found the following.

a) The thermalization depends on the phase of the Ising model and on whether the $\mathbb{Z}_2$ symmetry is preserved. For a system coupling operator σ^x, the symmetry is preserved and thermalization is produced in each symmetry sector, except in the paramagnetic limit where the interaction produces pure dephasing. Moreover, thermalization times are found to increase when approaching this limit for any configuration and spin number. For a system coupling operator $\sigma^x + \sigma^z$ (or simply σ^z) the symmetry is broken and the system thermalizes in the full Hilbert space. In the ferromagnetic limit, the symmetry-breaking component of the coupling, σ^z, has virtually no effect and the system thermalizes in each sector due to the action of σ^x.

b) Spins coupled to a common bath thermalize slower than spins coupled to independent baths, and the thermalization time increases with the number of spins and also depends on the system phase. This result suggest an interplay between collective effects leading in this case to subradiance and system correlations. Independent baths thermalize faster if all sites are coupled to a bath instead of only one site, but in both cases the thermalization time is highly dependent on the initial state. These results are supported by data from the spectrum of the Liouville operator and the time evolution of the Lindblad equation. Thus, we suggest the independent bath scenario to enhance thermalization or a common bath to suppress it and extend coherence times.

c) The thermalization time of atoms is structured in ϕ. For instance, for atoms coupled to a common reservoir the timescale shows a relative maximum around $0.3 \times \pi/2$ at $T = 0.51$. The presence of such maxima can be used as *sweet spots* to preserve coherence in the system away from the values of ϕ close to the ferromagnetic case.

d) The proposed neighborhood single-channel Lindblad operators designed for the ferromagnetic and paramagnetic limits gives rise to a thermal steady state only in a very narrow region around the extreme limits. However, even in these cases, it does not reproduce the correct decay rate given by the multi-channel Lindblad equation. Thus, the computationally intensive multi-channel Lindblad approach appears to be necessary to estimate many-body thermalization and decoherence times.

Our approach provides a clear path forward toward addressing pressing open problems suitable for near-term research projects, both within the present classical computational limits of 6-7 qubits imposed by the necessary multi-channel Lindblad approach, as well as the much larger system size that can be treated in experimental quantum simulator architectures. For instance, one may explore thermalization and decoherence control by varying the angle between the dipoles in the bath and the spins in the system in a common vs. independent reservoir scenario. In the latter, one could treat varying the dipole direction across the independent baths. The distance between the spins could also be changed to a non-equidistant spacing to reproduces what happens, for example, in one-dimensional ion traps. There are other questions which can be addressed within this framework, such as coupling to baths at different temperatures and the resulting equilibrium temperature and possible temperature gradients. Another extension to this research is to include long-range interactions in the system Hamiltonian. These long-range interactions present a correction to local tight-binding models such as the transverse quantum Ising model, occur in a number of experimental platforms, and can have significant effects on the statics and dynamics of a closed system

[28]. Could long-range effects in an open quantum system be used to control thermalization and decoherence times, and how would such control interact with different bath scenarios as in this study?

The validity of the secular approximation in many-body systems should also be revisited; the large number of possible transitions will increase the possibility of smaller differences between two transition frequencies for an increasing number of spins. Moreover, it remains an open question if the conclusions are altered when going beyond the Markov and weak coupling approximations. This question relates to whether thermalization is present in non-Markovian open quantum systems [68–70].

Relaxing these approximations can open the way to consider further experimental setups which are not covered by the approximations of the Lindblad equation. An example is a sympathetic cooling in ultracold atomic and molecular experiments [71, 72]. Ultracold molecules have been considered in the context of collisions leading to decoherence of the system [73, 74], which can be described with the Lindblad master equation. However, considering the bath as a quantum gas may allow one to explore Fermi vs. Bose statistics, by selecting the corresponding isotopes, or choosing a coupling which ranges from weakly to strongly interacting. Furthermore, some open systems cannot be described with a Markov approximation such as ladder-type structures where the system is of the same size as the bath [75], i.e., one rail representing the system, and the other the bath. Another example is that of a few nuclear spins of ^{13}C atoms surrounding a color center [76]. Future research may focus on local or neighborhood single-channel operators leading to the thermalization of the system, for and beyond the quantum Ising model. Such a step would help to move beyond seven spins and understand further the thermodynamic limit.

Acknowledgments – We gratefully appreciate discussions with K. Maeda, S. Montangero, G. Shchedrin, and N. C. Smith. This work was performed in part at the Aspen Center for Physics, which is supported by National Science Foundation grant PHY-1607611. This work was performed with partial support of the NSF under grants PHY-1806372, OAC-1740130, CCF-1839232, and the AFOSR under grant FA9550-14-1-0287. We acknowledge support of the U.K. Engineering and Physical Sciences Research Council (EPSRC) through the "Quantum Science with Ultracold Molecules" Programme (Grant No. EP/P01058X/1). The calculations were carried out using the high performance computing resources provided by the Golden Energy Computing Organization at the Colorado School of Mines. I.D.V. was financially supported by the Nanosystems Initiative Munich (NIM) under project No. 862050-2 and the DFG-grant GZ: VE 993/1-1.

[1] J. Eisert, M. Friesdorf, and C. Gogolin, "Quantum many-body systems out of equilibrium," Nature Physics **11**, 124 EP – (2015).
[2] Christian Gogolin and Jens Eisert, "Equilibration, thermalisation, and the emergence of statistical mechanics in closed quantum systems," Reports on Progress in Physics **79**, 056001 (2016).
[3] Heng-Na Xiong, Ping-Yuan Lo, Wei-Min Zhang, Da Hsuan Feng, and Franco Nori, "Non-Markovian complexity in the quantum-to-classical transition," Scientific Reports **5**, 13353 (2015).
[4] Magdalena Stobińska, Falk Töppel, Pavel Sekatski, and Adam Buraczewski, "Towards loophole-free Bell inequality test with preselected unsymmetrical singlet states of light," Phys. Rev. A **89**, 022119 (2014).
[5] A. Kossakowski, "On quantum statistical mechanics of non-Hamiltonian systems," Reports on Mathematical Physics **3**, 247 – 274 (1972).
[6] G. Lindblad, "On the generators of quantum dynamical semigroups," Communications in Mathematical Physics **48**, 119–130 (1976).
[7] Vittorio Gorini, Andrzej Kossakowski, and E. C. G. Sudarshan, "Completely positive dynamical semigroups of N-level systems," Journal of Mathematical Physics **17**, 821–825 (1976).
[8] Angel Rivas and Susana F. Huelga, *Open Quantum Systems* (Springer, Heidelberg Dordrecht London New York, 2012).
[9] Heinz-Peter Breuer and Francesco Petruccione, *The Theory of Open Quantum Systems*, 1st ed. (Clarendon Press, Oxford, 2009).
[10] Tomaz Prosen, "Third quantization: a general method to solve master equations for quadratic open Fermi systems," New Journal of Physics **10**, 043026 (2008).
[11] Tomaž Prosen and Marko Žnidarič, "Matrix product simulations of non-equilibrium steady states of

quantum spin chains," Journal of Statistical Mechanics: Theory and Experiment **2009**, P02035 (2009).
[12] Tomaz Prosen, "Exact Nonequilibrium Steady State of a Strongly Driven Open XXZ Chain," Phys. Rev. Lett. **107**, 137201 (2011).
[13] Mikel Palmero, Xiansong Xu, Chu Guo, and Dario Poletti, "Thermalization with detailed-balanced two-site Lindblad dissipators," ArXiv e-prints 1901.05145 (2019).
[14] Zi Cai and Thomas Barthel, "Algebraic versus exponential decoherence in dissipative many-particle systems," Phys. Rev. Lett. **111**, 150403 (2013).
[15] Andrew J. Daley, "Quantum trajectories and open many-body quantum systems," Advances in Physics **63**, 77–149 (2014).
[16] R. Rota, F. Storme, N. Bartolo, R. Fazio, and C. Ciuti, "Critical behavior of dissipative two-dimensional spin lattices," Phys. Rev. B **95**, 134431 (2017).
[17] Jean-Sébastien Bernier, Ryan Tan, Lars Bonnes, Chu Guo, Dario Poletti, and Corinna Kollath, "Light-cone and diffusive propagation of correlations in a many-body dissipative system," Phys. Rev. Lett. **120**, 020401 (2018).
[18] Patrick P. Hofer, Martí Perarnau-Llobet, L. David M. Miranda, Géraldine Haack, Ralph Silva, Jonatan Bohr Brask, and Nicolas Brunner, "Markovian master equations for quantum thermal machines: local versus global approach," New Journal of Physics **19**, 123037 (2017).
[19] G. Smith, J. A. Smolin, X. Yuan, Q. Zhao, D. Girolami, and X. Ma, "Quantifying coherence and entanglement via simple measurements," ArXiv e-prints 1707.09928 (2017).
[20] J. Onam González, Luis A. Correa, Giorgio Nocerino, José P. Palao, Daniel Alonso, and Gerardo Adesso, "Testing the validity of the 'local' and 'global' GKLS master equations on an exactly solvable model," Open Systems & Information Dynamics **24**, 1740010 (2017).
[21] Sina Hamedani Raja, Massimo Borrelli, Rebecca Schmidt, Jukka P. Pekola, and Sabrina Maniscalco, "Thermodynamic fingerprints of non-Markovianity in a system of coupled superconducting qubits," Phys. Rev. A **97**, 032133 (2018).
[22] Eduardo Mascarenhas, FranÃğois Damanet, Stuart Flannigan, Luca Tagliacozzo, Andrew J. Daley, John Goold, and InÃl's de Vega, "Nonreciprocal quantum transport at junctions of structured leads," ArXiv e-prints 1810.04929 (2018).
[23] Ernst Ising, "Beitrag zur Theorie des Ferromagnetismus," Zeitschrift für Physik **31**, 253–258 (1925).
[24] Subir Sachdev, *Quantum Phase Transitions*, 2nd ed. (Cambridge University Press, Cambridge, United Kingdom, 2011).
[25] Amit Dutta and J. K. Bhattacharjee, "Phase transitions in the quantum Ising and rotor models with a long-range interaction," Phys. Rev. B **64**, 184106 (2001).
[26] Thomas Koffel, M. Lewenstein, and Luca Tagliacozzo, "Entanglement entropy for the long-range Ising chain in a transverse field," Phys. Rev. Lett. **109**, 267203 (2012).
[27] Davide Vodola, Luca Lepori, Elisa Ercolessi, and Guido Pupillo, "Long-range Ising and Kitaev models: phases, correlations and edge modes," New Journal of Physics **18**, 015001 (2016).
[28] Daniel Jaschke, Kenji Maeda, Joseph D Whalen, Michael L Wall, and Lincoln D Carr, "Critical phenomena and Kibble-Zurek scaling in the long-range quantum Ising chain," New Journal of Physics **19**, 033032 (2017).
[29] Malte Vogl, Gernot Schaller, and Tobias Brandes, "Criticality in transport through the quantum Ising chain," Phys. Rev. Lett. **109**, 240402 (2012).
[30] Michael L. Wall, Kenji Maeda, and Lincoln D. Carr, "Simulating quantum magnets with symmetric top molecules," Annalen der Physik **525**, 845–865 (2013).
[31] M. L. Wall, K. Maeda, and Lincoln D. Carr, "Realizing unconventional quantum magnetism with symmetric top molecules," New Journal of Physics **17**, 025001 (2015).
[32] A. Lewenstein, M. Sanpera, V. Ahufinger, B. Damski, A. Sen De, and U. Sen, "Ultracold atomic gases in optical lattices: Mimicking condensed matter physics and beyond," Adv. Phys. **56**, 243–379 (2007).
[33] J. G. Bohnet, B. C. Sawyer, J. W. Britton, M. L. Wall, A. M. Rey, M. Foss-Feig, and J. J. Bollinger, "Quantum spin dynamics and entanglement generation with hundreds of trapped ions," Science **352**, 1297–1301 (2016).
[34] H. Labuhn, D. Barredo, S. Ravets, S. de Léséleuc, T. Macrì, T. Lahaye, and A. Browaeys, "Tunable two-dimensional arrays of single Rydberg atoms for realizing quantum Ising models," Nature **534**, 667–670 (2016).
[35] Thomas Häner and Damian S. Steiger, "0.5 Petabyte Simulation of a 45-qubit Quantum Circuit," in *Proceedings of the International Conference for High Performance Computing, Networking, Storage and Analysis*, SC '17 (ACM, New York, NY, USA, 2017) pp. 33:1–33:10.
[36] E. Pednault, J. A. Gunnels, G. Nannicini, L. Horesh, T. Magerlein, E. Solomonik, and R. Wisnieff, "Breaking the 49-Qubit Barrier in the Simulation of Quantum Circuits," ArXiv e-prints 1710.05867 (2017).

[37] Zhao-Yun Chen, Qi Zhou, Cheng Xue, Xia Yang, Guang-Can Guo, and Guo-Ping Guo, "64-qubit quantum circuit simulation," Science Bulletin (2018), 10.1016/j.scib.2018.06.007.

[38] Berislav Buca and Tomaz Prosen, "A note on symmetry reductions of the Lindblad equation: transport in constrained open spin chains," New Journal of Physics **14**, 073007 (2012).

[39] R. H. Lehmberg, "Radiation from an N-Atom System. I. General Formalism," Phys. Rev. A **2**, 883–888 (1970).

[40] Massimo Ostilli and Carlo Presilla, "Thermalization of noninteracting quantum systems coupled to blackbody radiation: A Lindblad-based analysis," Phys. Rev. A **95**, 062112 (2017).

[41] Gernot Schaller, *Open Quantum Systems Far from Equilibrium* (Springer, 2014).

[42] Michael A. Nielsen and Isaac L. Chuang, *Quantum Computation and Quantum Information*, 9th ed. (Cambridge Univ. Press, Cambridge, United Kingdom, 2007).

[43] Victor V. Albert and Liang Jiang, "Symmetries and conserved quantities in Lindblad master equations," Phys. Rev. A **89**, 022118 (2014).

[44] D. Manzano and P. I. Hurtado, "Harnessing symmetry to control quantum transport," Advances in Physics **67**, 1–67 (2018).

[45] M. S. Sarandy and D. A. Lidar, "Adiabatic approximation in open quantum systems," Phys. Rev. A **71**, 012331 (2005).

[46] Birger Horstmann, J. Ignacio Cirac, and Géza Giedke, "Noise-driven dynamics and phase transitions in fermionic systems," Phys. Rev. A **87**, 012108 (2013).

[47] D. Jaschke and L. D. Carr, "Open source Matrix Product States: Exact diagonalization and other entanglement-accurate methods revisited in quantum systems," ArXiv e-prints 1802.10052 (2018).

[48] "Open Source Matrix Product States (OpenMPS)," http://sourceforge.net/projects/openmps/, last visited Feb 17, 2019.

[49] John Cardy, *Scaling and Renormalization in Statistical Physics* (Cambridge University Press, 2003).

[50] R. H. Dicke, "Coherence in spontaneous radiation processes," Phys. Rev. **93**, 99–110 (1954).

[51] William Guerin, Michelle O. Araújo, and Robin Kaiser, "Subradiance in a large cloud of cold atoms," Phys. Rev. Lett. **116**, 083601 (2016).

[52] A. Asenjo-Garcia, M. Moreno-Cardoner, A. Albrecht, H. J. Kimble, and D. E. Chang, "Exponential improvement in photon storage fidelities using subradiance and "selective radiance" in atomic arrays," Phys. Rev. X **7**, 031024 (2017).

[53] David Plankensteiner, Christian Sommer, Michael Reitz, Helmut Ritsch, and Claudiu Genes, "Enhanced collective purcell effect of coupled quantum emitter systems," ArXiv e-prints 1811.03442 (2018).

[54] G. Facchinetti, S. D. Jenkins, and J. Ruostekoski, "Storing light with subradiant correlations in arrays of atoms," Phys. Rev. Lett. **117**, 243601 (2016).

[55] Janne Ruostekoski and Juha Javanainen, "Arrays of strongly coupled atoms in a one-dimensional waveguide," Phys. Rev. A **96**, 033857 (2017).

[56] Giuseppe Fiscelli, Roberta Palacino, Roberto Passante, Lucia Rizzuto, Salvatore Spagnolo, and Wenting Zhou, "Time-dependent resonance interaction energy between two entangled atoms under nonequilibrium conditions," Phys. Rev. A **98**, 042506 (2018).

[57] Lincoln D. Carr, David DeMille, Roman V. Krems, and Jun Ye, "Cold and ultracold molecules: science, technology and applications," New Journal of Physics **11**, 055049 (2009).

[58] R. Schmied, T. Roscilde, V. Murg, D. Porras, and J. I. Cirac, "Quantum phases of trapped ions in an optical lattice," New Journal of Physics **10**, 045017 (2008).

[59] M. Everitt, J. Dunningham, and B. T. Varcoe, "Quantum computing with Rydberg atoms in cavities," in *Frontiers in Optics 2009/Laser Science XXV/Fall 2009 OSA Optics & Photonics Technical Digest* (Optical Society of America, 2009) p. FThU3.

[60] Hashem Zoubi and Helmut Ritsch, "Chapter 3 - excitons and cavity polaritons for optical lattice ultracold atoms," in *Advances in Atomic, Molecular, and Optical Physics*, Advances In Atomic, Molecular, and Optical Physics, Vol. 62, edited by Ennio Arimondo, Paul R. Berman, and Chun C. Lin (Academic Press, 2013) pp. 171 – 229.

[61] C. F. R. Mateus, M. C. Y. Huang, Yunfei Deng, A. R. Neureuther, and C. J. Chang-Hasnain, "Ultrabroadband mirror using low-index cladded subwavelength grating," IEEE Photonics Technology Letters **16**, 518–520 (2004).

[62] A. Recati, P. O. Fedichev, W. Zwerger, J. von Delft, and P. Zoller, "Atomic quantum dots coupled to a reservoir of a superfluid Bose-Einstein condensate," Phys. Rev. Lett. **94**, 040404 (2005).

[63] Peter P. Orth, Ivan Stanic, and Karyn Le Hur, "Dissipative quantum Ising model in a cold-atom spin-boson mixture," Phys. Rev. A **77**, 051601 (2008).

[64] Inés de Vega, Diego Porras, and J. Ignacio Cirac, "Matter-wave emission in optical lattices: Single particle and collective effects," Phys. Rev. Lett. **101**, 260404 (2008).

[65] Michael Stewart, Ludwig Krinner, Arturo Pazmiño, and Dominik Schneble, "Analysis of non-

Markovian coupling of a lattice-trapped atom to free space," Phys. Rev. A **95**, 013626 (2017).
[66] Yiwen Chu, Prashanta Kharel, William H. Renninger, Luke D. Burkhart, Luigi Frunzio, Peter T. Rakich, and Robert J. Schoelkopf, "Quantum acoustics with superconducting qubits," Science **358**, 199–202 (2017).
[67] Jamir Marino, Alessio Recati, and Iacopo Carusotto, "Casimir forces and quantum friction from Ginzburg radiation in atomic Bose-Einstein condensates," Phys. Rev. Lett. **118**, 045301 (2017).
[68] Ángel Rivas, Susana F. Huelga, and Martin B. Plenio, "Quantum non-Markovianity: characterization, quantification and detection," Reports on Progress in Physics **77**, 094001 (2014).
[69] Heinz-Peter Breuer, Elsi-Mari Laine, Jyrki Piilo, and Bassano Vacchini, "Colloquium: Non-Markovian dynamics in open quantum systems," Rev. Mod. Phys. **88**, 021002 (2016).
[70] Inés de Vega and Daniel Alonso, "Dynamics of non-Markovian open quantum systems," Rev. Mod. Phys. **89**, 015001 (2017).
[71] L. D. Carr, T. Bourdel, and Y. Castin, "Limits of sympathetic cooling of fermions by zero-temperature bosons due to particle losses," Phys. Rev. A **69**, 033603–1–14 (2004).
[72] Jongseok Lim, Matthew D. Frye, Jeremy M. Hutson, and M. R. Tarbutt, "Modeling sympathetic cooling of molecules by ultracold atoms," Phys. Rev. A **92**, 053419 (2015).
[73] C. J. Hemming and R. V. Krems, "Collisional decoherence of internal-state superpositions in a trapped ultracold gas," Phys. Rev. A **81**, 052701 (2010).
[74] Eric Braaten, H.-W. Hammer, and G. Peter Lepage, "Lindblad equation for the inelastic loss of ultracold atoms," Phys. Rev. A **95**, 012708 (2017).
[75] Adam M. Kaufman, M. Eric Tai, Alexander Lukin, Matthew Rispoli, Robert Schittko, Philipp M. Preiss, and Markus Greiner, "Quantum thermalization through entanglement in an isolated many-body system," Science **353**, 794–800 (2016).
[76] Benjamin Smeltzer, Lilian Childress, and Adam Gali, "^{13}C hyperfine interactions in the nitrogen-vacancy centre in diamond," New Journal of Physics **13**, 025021 (2011).

Appendix A: Thermalization for odd symmetry sector and $S_k = \sigma_k^z$

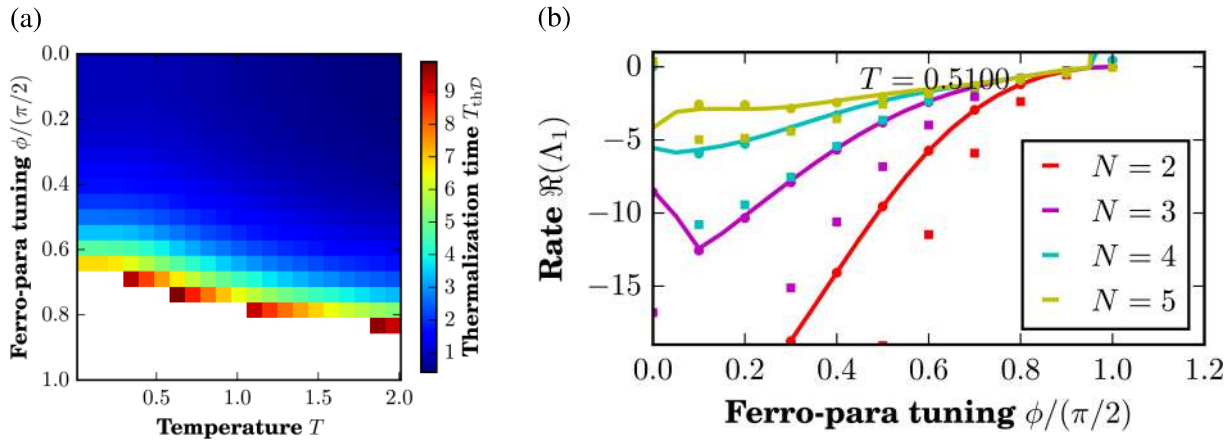

FIG. 7. *Summary for the odd symmetry sector.* (a) Thermalization timescale for the odd symmetry sector via the trace distance. We observe the same trend as in the even sector, i.e., the timescale becomes longer toward the paramagnetic limit. Time evolution for $\tau = 10$; white regions do not meet criterion within this time. (b) Rate and timescales for different system sizes for the global multi-channel approach and initial states. The curves represent the closing rate toward the paramagnetic limit and for growing system size. A random initial state (circles) matches this rate of the Liouville operator $\mathcal{L}$; the ground state (squares) as the initial state thermalizes faster.

So far, we have considered the analysis of the system in the even symmetry sector of the $\mathbb{Z}_2$ symmetry. We summarize the odd sector in this brief appendix. We expect similar behavior. The thermalization time $T_{\mathrm{th}\mathcal{D}}$ slows down toward the paramagnetic limit, see Fig. 7(a) for multi-channel Lindblad operators in scenario (a). If we consider increasing system size N within the

same setup, we note that the gap is closing for an increasing number of spins. The initial state has an equal effect on the timescale as in the even sector: the ground state (squares) has a shorter thermalization time than the random initial state (circles); the latter match the gap $\Re(\Lambda_1)$ in the spectrum of the Liouville operator $\mathcal{L}$. We conclude from these two examples that the features presented in our work are not unique to the choice of the symmetry sector.

Appendix B: Multi-channel Lindblad equation

In this appendix, we present a more detailed description of the multi-channel approach. We will specify the component $\gamma(E_{ba}, \mathbf{r}_{jk})$ present in the decay rates of the Lindblad equation, see Eq. (12). Using standard notation, we denote the transition frequency $\omega = E_{ba}$. As discussed in [39], for the light-matter interaction the function $\gamma(E_{ba}, \mathbf{r}_{jk})$ takes the form

$$\gamma(\omega, 0) = \tilde{n}(\omega) \underbrace{\frac{4\omega^3 d_{\text{dip}}^2}{3c^3}}_{=\Gamma_0} = \tilde{n}(\omega)\Gamma_0\,, \tag{B1}$$

for the case $j = k$, where c is the speed of light. For non-zero spatial distance, it is found that

$$\gamma(\omega, r_{jk}) = \tilde{n}(\omega)\Gamma_0 \Re\big(\chi(\omega, \mathbf{r}_{jk})\big), \tag{B2}$$

where

$$\chi(\omega, \mathbf{r}_{jk}) = \left((1-\xi^2)\frac{-\mathrm{i}\mathrm{e}^{\mathrm{i}\omega r_{jk}}}{\omega r_{jk}} + (1-3\xi^2)\left(\frac{\mathrm{e}^{\mathrm{i}\omega r_{jk}}}{(\omega r_{jk})^2} + \frac{\mathrm{i}\mathrm{e}^{\mathrm{i}\omega r_{jk}}}{(\omega r_{jk})^3}\right)\right). \tag{B3}$$

Here we assume for simplicity that the spin dipoles in the bath are aligned orthogonally to the Ising chain, which leads to $\xi \equiv (\mathbf{d}_{\text{dip}} \cdot \mathbf{r}_{jk})/(d_{\text{dip}} r_{jk}) = 0$, with $r_{ij} = |\mathbf{r}_{ij}|$. We note that different choices of dipole orientation lead to different spatial decays for spin-spin correlations within the dissipation process. For instance, if the dipoles and spin locations are parallel, we find $\xi = 1$, and therefore the first term in Eq. (B2) cancels while the second and third order term in $1/r_{jk}$ survive. This would lead to spin-spin correlations that decay faster with their distance than in cases where the first slower decaying term is present. In contrast, for $\xi = 1/\sqrt{3}$, the second and third order terms in $1/r_{jk}$ is set to zero, while the slower decaying term remains with a pre-factor of $2/3$. This case is apart from the pre-factors such as Γ_0, as in the case of spins coupled to a BEC, and shows the versatility with which this system can be tuned. We ran simulations similar to Fig. 4(a) for selected values of ξ and observed the same behavior, i.e., the thermalization timescale slows down for more spins. Furthermore, we have defined $\tilde{n}(\omega)$ as

$$\tilde{n}(\omega) = \begin{cases} n(\omega)\,, & \forall\omega > 0\,, \\ 1 + n(-\omega)\,, & \forall\omega < 0\,. \end{cases} \tag{B4}$$

where $n(\omega) = 1/(e^{\beta\omega - 1} - 1)$, and $\beta = 1/k_{\text{B}}T$, with k_{B} the Boltzmann constant. Finally, we neglect for simplicity the Lamb shift-like terms that come from the imaginary part of $\chi(\omega, \mathbf{r}_{jk})$, since these terms will not contribute to the dissipative timescales and the thermalization process we aim to analyze here.

Appendix C: Deriving the neighborhood single-channel Lindblad operators

We introduce the neighborhood single-channel Lindblad operators in this section.

1. Neighborhood single-channel operators in the paramagnetic limit

To derive the simpler Lindblad operators that in the paramagnetic limit give rise to thermalization, we consider solely for this subsection $S_k = \sigma_k^z$. For the paramagnetic limit the eigenstates are product states of local eigenstates of the Pauli matrices, i.e., product states of spins aligned and anti-aligned with the external field. The Schmidt decomposition of a product state has exactly one non-zero singular value, e.g., $\lambda_{1ka} = 1$, and therefore Eq. (14) reduces drastically such that

$$ {}^{ij'}\mathcal{F}_{ab}^{[k]} = \underbrace{\left\langle a_k^{i'=1}\right| S_k \left|b_k^{j=1}\right\rangle}_{(I)} \underbrace{\left\langle a_{\bar{k}}^{i'=1}\middle| b_{\bar{k}}^{j=1}\right\rangle}_{(II)}, \lambda_1 = \lambda_1' = 1\,, \tag{C1} $$

with all other Schmidt values being zero. In order to contribute, both terms (I) and (II) should be non-zero. Moreover, since we use an orthogonal set of basis vectors for k and $\bar{k}$ each of the terms is either 0 or 1. The term (I) marked in Eq. (C1) is equal to one if $\left\langle a_k^{i'=1}\right|$ and $\left|b_k^{j=1}\right\rangle$ are anti-aligned as S_k flips the spin. The term (II) from Eq. (C1) is equal to one if the sites $k' \neq k$ do not change their state. Thus, we obtain that the Lindblad operator for each site, producing cooling of the system is

$$ L^{[k]} = \left|\uparrow_x\right\rangle_k \left\langle\downarrow_x\right|_k\,, \tag{C2} $$

while $(L^{[k]})^\dagger$ produces heating, respectively. The state on site k aligned with the external field in the x-direction is $\left|\uparrow_x\right\rangle_k$, while the state anti-aligned is $\left|\downarrow_x\right\rangle_k$. Therefore, the Lindblad operator in Eq. (C2) aligns the spin k with the external field and brings this spin to the ground state of the paramagnetic limit. A numerical implementation of this case is discussed in App. D.

2. Neighborhood single-channel operators in the ferromagnetic limit

To develop the single-channel operators for the ferromagnetic limit, we return to the coupling $S_k = \sigma_k^x$. On the one hand, we know that the eigenstates are not entangled, i.e., $\lambda_j = 0$ for $j \neq 1$ but degenerate. For instance, the ground state subspace contains two degenerate, symmetry-broken eigenstates, $|\uparrow\cdots\uparrow\rangle$ and $|\downarrow\cdots\downarrow\rangle$. Thus, we do not use the $\mathbb{Z}_2$ symmetry for this setup. We neglect for simplicity the edges of the chain. The first excited subspace corresponds to a set of $2(N-2)$ degenerate states with an energy 4 with respect to the ground state. These are the excited states which can be reached after an action of a single Lindblad operator from one of the ground states. The states contain two domain walls which separate a phase of spins $\uparrow$ (or $\downarrow$) from a background phase of spins oriented in the opposite direction. In a similar way, the second excited subspace will be composed of states with four domain walls, and an energy 8 with respect to the ground state. In general, the different energy subspaces will correspond to eigenstates having an increasing number of magnetic domains.

On the other hand, from the spectral decomposition of the coupling operator in Eq. (14) and the multi-channel Lindblad equation, we know that (i) σ_k^x only connects eigenstates separated by a single spin flip, and (ii) in the Lindblad equation only transitions with $\gamma(\omega \neq 0, \mathbf{r}_{jk})$ will contribute, since $\gamma(0, \mathbf{r}_{jk}) = 0$. In other words, Lindblad operators that do not change the energy will not be taken into account. Hence, both conditions imply that Lindblad operators should connect eigenstates that differ in a single spin flip and contain a different number of magnetic domains, i.e., correspond to a different energy.

With this prescription, the simplest choice are Lindblad operators defined on a neighborhood of up to three sites. Depending on whether they increase or decrease the number of magnetic domains, they will be associated with heating or cooling. In detail, we define the states $|m\rangle_k = |\uparrow\uparrow\uparrow\rangle_k$, $|o\rangle_k = |\uparrow\downarrow\uparrow\rangle_k$, $|r\rangle_k = |\downarrow\uparrow\downarrow\rangle_k$, and $|t\rangle_k = |\downarrow\downarrow\downarrow\rangle_k$ on the three neighboring sites $k-1, k, k+1$. We can now define a generic Lindblad operator $L_{ab}^{[k]} = |a\rangle_k \langle b|_k$ acting on the bulk of the system

on a three-site neighborhood. In detail, the heating Lindblad operators have the form

$$L_{rt}^{[k]} = |r\rangle_k \langle t|_k \ , \ L_{om}^{[k]} = |o\rangle_k \langle m|_k \ , \tag{C3}$$

for $k = 2, \ldots, N-1$, and give rise to an increase in energy. Each of these Lindblad operators can be interpreted as a spin flip with one or two control-spins. Furthermore, for the boundary sites, we define two-site states $|u\rangle_k = |\uparrow\uparrow\rangle_k$, $|v\rangle_k = |\downarrow\uparrow\rangle_k$, $|w\rangle_k = |\uparrow\downarrow\rangle_k$, and $|x\rangle = |\downarrow\downarrow\rangle_k$ for the sites k and $k+1$. The corresponding Lindblad operators are $L_{wx}^{[1]}$, $L_{vu}^{[1]}$, $L_{vx}^{[N-1]}$, and $L_{wu}^{[N-1]}$ for the boundary sites. The cooling operators then correspond to their Hermitian conjugates, i.e.,

$$L_{tr}^{[k]} = |t\rangle_k \langle r|_k \ , \ L_{mo}^{[k]} = |m\rangle_k \langle o|_k \ , \tag{C4}$$

for $k = 2, \ldots, N-1$, and $L_{xw}^{[1]}$, $L_{uv}^{[1]}$, $L_{xv}^{[N-1]}$, and $L_{uw}^{[N-1]}$ for the boundary sites. As mentioned above, each operation in the bulk of the system introduces an energy difference of ± 4, while at the boundaries the energy change will only be ± 2.

3. Neighborhood single-channel operators in between the limits

We explored as well the possibility of using the neighborhood single-channel Lindblad operators from both limits to capture the region between the limits with $0 < \phi < \pi/2$. An optimization over the ratio of the two coupling strengths, i.e., the coupling strength for the neighborhood single-channel Lindblad operators from the ferromagnetic limit and the local single-channel Lindblad operators for the paramagnetic limit, did not lead to trace distances close to the steady state. For example, the trace distances for values of $\phi \approx \pi/4$ do not drop below 0.1. This result indicates that the multi-channel approach is required to determine thermalization in interacting many-body systems unless non-trivial approximations yet to be discovered can simplify dynamics to neighborhood single-channel Lindblad operators.

Appendix D: Thermalization for $S_k = \sigma_k^z$

Up to now, all the numerical calculations in the paper have considered the system coupling operator as $S_k = \sigma_k^x$. However, in this appendix, we analyze the case $S_k = \sigma_k^z$. We have some obvious changes associated with this choice. (i) The paramagnetic limit can now thermalize as the eigenstates of the paramagnetic limit do not correspond to the eigenstates of S_k. In contrast, thermalization in the ferromagnetic limit suffers from the same effect as before in which the Lindblad operators induce dephasing, but no transitions. (ii) The $\mathbb{Z}_2$ symmetry is broken by the Lindblad operator, and there is no distinction between the odd and the even sector for the choice of $S_k = \sigma_k^z$.

We present in Fig. 8 the data corresponding to our main scenario (a) and consider the multi-channel Lindblad operators. Figure 8(a) shows the thermalization timescale $T_{\text{th}\mathcal{D}}$ for the multi-channel approach, as defined in Eq. (20). We observe the opposite behavior from before, as expected: the ferromagnetic limit now has a slow timescale indicated by the white regions where the criterion is not met within $\tau = 10$. We study the gap as a function of the system size in Fig. 8(b), where the gap of the Liouville operator decreases for larger system sizes comparing $N = 2, 3$ and 4. Thus, analogous to Figure 4(a), we find that the thermalization timescale also slows down for larger systems in this case.

We now consider the single channel Lindblad operators derived in Sec. C for the paramagnetic limit, which are given by Eq. (C2) for cooling the system, while its Hermitian conjugate heats it. To rephrase the operators in terms of the transition between states according to Eq. (6), we would define the states $|y\rangle = |\uparrow\rangle_k$ and $|z\rangle = |\downarrow\rangle_k$ and the corresponding Lindblad operators $L_{yz}^{[k]}$ and $L_{zy}^{[k]}$. The corresponding energy difference used to calculate the rates is $\Delta = \pm 2g$. These Lindblad operators correspond to spin raising and lowering operators in the x-direction, and therefore they are similar to the single-channel approaches usually considered in the literature [14–17]. Figure 8(c) shows that indeed the chosen single-channel operators thermalize the system in the paramagnetic

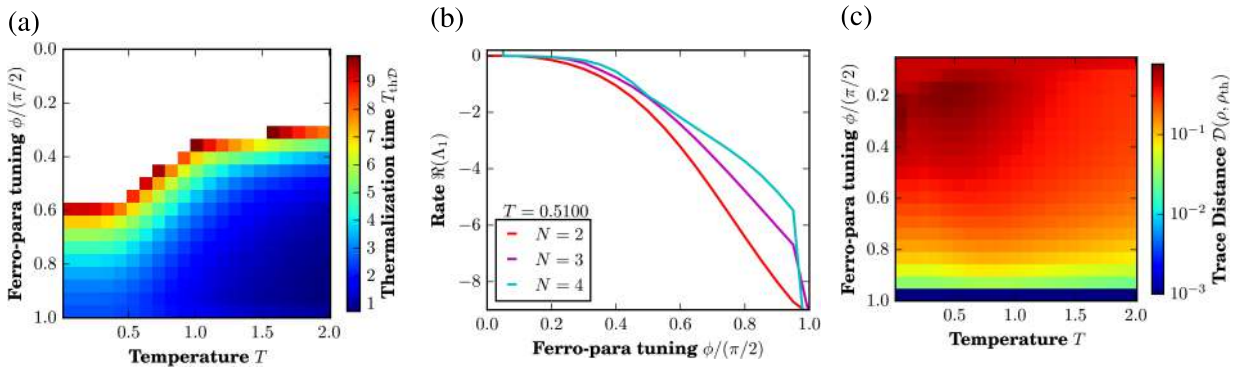

FIG. 8. *Summary for operator $S_k = \sigma_k^z$ in the interaction Hamiltonian.* (a) The thermalization time $T_{\mathrm{th}\mathcal{D}}$ determined via the trace distance exhibits longer timescales toward the ferromagnetic limit. White areas indicate thermalization times beyond $\tau = 10$. (b) The rate of the Liouville operator for the multi-channel approach with a common bath with growing system size. The rate decreases toward the ferromagnetic limit and decreases for increasing system sizes. (c) We choose the neighborhood single-channel Lindblad operators designed for the paramagnetic limit on a system of $L = 4$. We observe that the system only thermalizes in the limit $\phi = \pi/2$ and these operators cannot be used apart from $\phi = \pi/2$. Here, we consider the final state of the time evolution with $\tau = 10$ starting from a random initial state. The rate has non-zero values around $\phi \approx \pi/2$ and does not prevent thermalization.

limit. The distance to the thermal state in the limit $\phi = \pi/2$ is below 10^{-12}, but we set the minimal trace distance artificially to 10^{-3} for better visualization of the gradient around the limit.